remote sensing

MDPI

Technical Note

Quantitative Analysis of Forest Fires in Southeastern Australia Using SAR Data

Aqil Tariq [1], Hong Shu [1], Qingting Li [2], Orhan Altan [3], Mobushir Riaz Khan [4], Muhammad Fahad Baqa [5] and Linlin Lu [5,*]

[1] State Key Laboratory of Information Engineering in Surveying, Mapping and Remote Sensing (LIESMARS), Wuhan University, Wuhan 430079, China; aqiltariq@whu.edu.cn (A.T.); shu_hong@whu.edu.cn (H.S.)
[2] Airborne Remote Sensing Center, Aerospace Information Research Institute, Chinese Academy of Sciences, Beijing 100094, China; liqt@radi.ac.cn
[3] Department of Geomatics, Istanbul Technical University, Istanbul 36626, Turkey; oaltan@itu.edu.tr
[4] School of Environmental Science, Charles Sturt University, Albury-Wodonga 2640, Australia; mobkhan@csu.edu.au
[5] Key Laboratory of Digital Earth Science, Aerospace Information Research Institute, Chinese Academy of Sciences, Beijing 100094, China; 2252293808@mails.ucas.edu.cn
* Correspondence: lull@radi.ac.cn

Abstract: Prescribed burning is a common strategy for minimizing forest fire risk. Fire is introduced under specific environmental conditions, with explicit duration, intensity, and rate of spread. Such conditions deviate from those encountered during the fire season. Prescribed burns mostly affect surface fuels and understory vegetation, an outcome markedly different when compared to wildfires. Data on prescribed burning are crucial for evaluating whether land management targets have been reached. This research developed a methodology to quantify the effects of prescribed burns using multi-temporal Sentinel-1 Synthetic Aperture Radar (SAR) imagery in the forests of southeastern Australia. C-band SAR datasets were specifically used to statistically explore changes in radar backscatter coefficients with the intensity of prescribed burns. Two modeling approaches based on pre- and post-fire ratios were applied for evaluating prescribed burn impacts. The effects of prescribed burns were documented with an overall accuracy of 82.3% using cross-polarized backscatter (VH) SAR data under dry conditions. The VV polarization indicated some potential to detect burned areas under wet conditions. The findings in this study indicate that the C-band SAR backscatter coefficient has the potential to evaluate the effectiveness of prescribed burns due to its sensitivity to changes in vegetation structure.

Keywords: prescribed burns; SAR; fire impact; radar burn ratio; post-fire restoration; change detection

Citation: Tariq, A.; Shu, H.; Li, Q.; Altan, O.; Khan, M.R.; Baqa, M.F.; Lu, L. Quantitative Analysis of Forest Fires in Southeastern Australia Using SAR Data. *Remote Sens.* **2021**, *13*, 2386. https://doi.org/10.3390/rs13122386

Academic Editors: Alfonso Fernández-Manso and Carmen Quintano

Received: 10 May 2021
Accepted: 17 June 2021
Published: 18 June 2021

1. Introduction

Wildfires are a global agent for environmental change [1,2], and prescribed burning is an important strategy to minimize the harmful impact of wildfires globally [3]. Prescribed burning has proven effective in various regions, including Southern Europe [4], North America [5,6], and Australia [7–9]. In order to meet particular environmental protection targets, controlled fires are required for prescribed burning. A fire is set under specific environmental conditions, over an explicit region, and with a specific length, intensity, and spread rate [3]. Prescribed burning was first implemented in forests with the aim of minimizing wildfire risks in Australia in the late 1950s [9]. The prescribed fire is used for: (i) fuel reduction to moderate the adverse effects of wildfires on biodiversity, water, and soil [10–12], and (ii) land management [13], including logging restoration, forest maintenance, and conservation of biodiversity [14].

The intensity of prescribed burns varies between low to moderate in southeastern Australia [15]. The rate of fire spread depends on the seasons. For example, there are

fewer fire ignitions in spring, which is from September to December, whereas there are more ignitions in autumn, from March to May, when weather conditions are mild. Broad-scale adoption of prescribed burning as a conservation measure has altered the structure and pattern of the fuel period, substantially decreasing the frequency and magnitude of unplanned fires, along with the severity of impacts on land, environmental factors, and vegetation in this area [9,11]. However, the effects of prescribed burning should be monitored to confirm whether defined consumption, area coverage, and fire intensity levels were achieved. In various habitats, coarse woody debris is a crucial structural feature for forest biodiversity and functioning [16], and can be impacted by the burning season, severity, and frequency of prescribed fire treatments [17,18]. Historical data on prescribed burning effects expressed as intensity or severity of fire are important for determining the degree to which the goals of land/wildfire management have been accomplished and also for informing the reporting process aimed at quantifying atmospheric emissions from fire.

The degree or magnitude of environmental changes caused by fire can be defined as the severity of fire and can be calculated by bio-loss [19]. These environmental trends are generally measured by severity indices, including the Composite Burn Index (CBI), to assess the rate of burning for vegetation areas in various sections [20]. Nevertheless, field investigations are expensive and their application over large areas is impractical. Remote sensing methods have been widely used to collect information on post-fire landscape conditions over broad spatial scales [21–23], and spectral indices from multi-spectral remote sensing data are commonly used for assessing burn severity at the spatial grain of the sensor [24,25]. However, reflectance-based indices have difficulty in yielding accurate results due to the influence of multiple factors, such as forest sensitivity, plant phenology, or solar elevation, rather than structure [26,27].

Considering their sensitivity to scattering elements and capacity to provide direct measurements of vegetation structure, active sensors such as radar and LiDAR may overcome the above limitations [28,29]. Various SAR-based techniques are useful to examine the effects of fire on the three-dimensional structures of canopy and the strata of lower plants, as radar waves have the ability to penetrate through canopy. The possibility to estimate the effects of forest fires via radar-based measurements, such as polarimetric decomposition coefficients, interferometric coherence, and backscatter intensities, has been demonstrated in previous studies [30,31]. These studies obtained satisfactory estimation accuracies in wildfire-affected forests and emphasized the need for model calibration with reference datasets. Burned area algorithms based on temporal differences between pre- and post-fire radar backscatter values may also suffer from the temporal decorrelation effect that must also be accounted for. A recent study also revealed that undesirable effects caused by topography and varying environmental circumstances could be minimized with bi-temporal approaches [30].

Since prescribed burns primarily affect surface fuels and understory vegetation, their effect on radar backscattering is largely unknown and may vary from that of wildfires. The feasibility of analysis methods developed for wildfires has barely been evaluated when applied to controlled burns. Due to the introduction of thresholds for distinguishing different groups of fires categorized by their severity, their applications are further complicated. In addition, it is difficult to distinguish between high-intensity wildfire events and controlled burns, where the impact of fire ranges from low to moderate. Since SAR data provide a wealth of information on fire effects even for fires at low severity levels, C-band SAR data hold great potential for assessing the impacts of prescribed burns [22]. The objectives of this study include developing and applying a framework for forest fire analysis in areas impacted by controlled burns, and evaluating the effect of SAR sensor polarization and environmental conditions on analysis in comparison with wildfires.

2. Study Area

This study was conducted in Croajingolong National Park in southeastern Australia (36°13′30″ S to 39°24′42″ S, 149°47′53″ E to 150°18′12″) (Figure 1) [32]. One of only twelve

world biosphere reserves in Australia, Croajingolong National Park in the state of Victoria is adjacent to Nadgee Nature Reserve in New South Wales. The study area has an oceanic Mediterranean climate with mean annual precipitation of about 1200 mm, which can be divided into a warm and dry season (October to April) and a cool and wet season (May to September) with >70% of precipitation [33]. The monthly average temperature can be as high as 27.2 °C, usually in January [34]. The above-ground biomass (AGB) ranges between 250 and 350 t/ha for mature Croajingolong National Park, with a further tall woody understory of 10–20 t/ha and woody debris of 50–70 t/ha. Southeastern Australia's forests in Croajingolong are distinguished by breeding plants (70% of the species, specifically the main species of tree) from post-fire stems [35]. With high-intensity fires, the trees may withstand defoliation, destruction of stem, and total top scorch, and some particular trees regenerate apically dominant crowns within five years. Within a month of burning, epicormics shoots emerge when fire-destroyed branches and upper stem parts weakened by fire eventually split and fall within the first two years. Fire-defoliated crowns of trees are typically destroyed, with shoots of epicormics restricted to the lower stem. With 35% to 45% of the total trees impacted by complete crown scorch, crown mortality also occurs. Depending on the species, crown replacement is between 30% and 95% within five years, and it is impossible to differentiate plants with substituted tops from those that have not experienced top death. In the lesser plant layers, up to 85% of classes can achieve flowering in the first two years after prescribed burns. Therefore, in the first year after the fire, certain improvements in forest composition can be predicted, as leaves emerge from the stem and main branches of both eucalyptus and shrub plants. Between 11 November and 30 December 2019, a scheduled burn was carried out, and approximately 88,500 hectares of tall open karri forest were burned in Croajingolong (Figure 1).

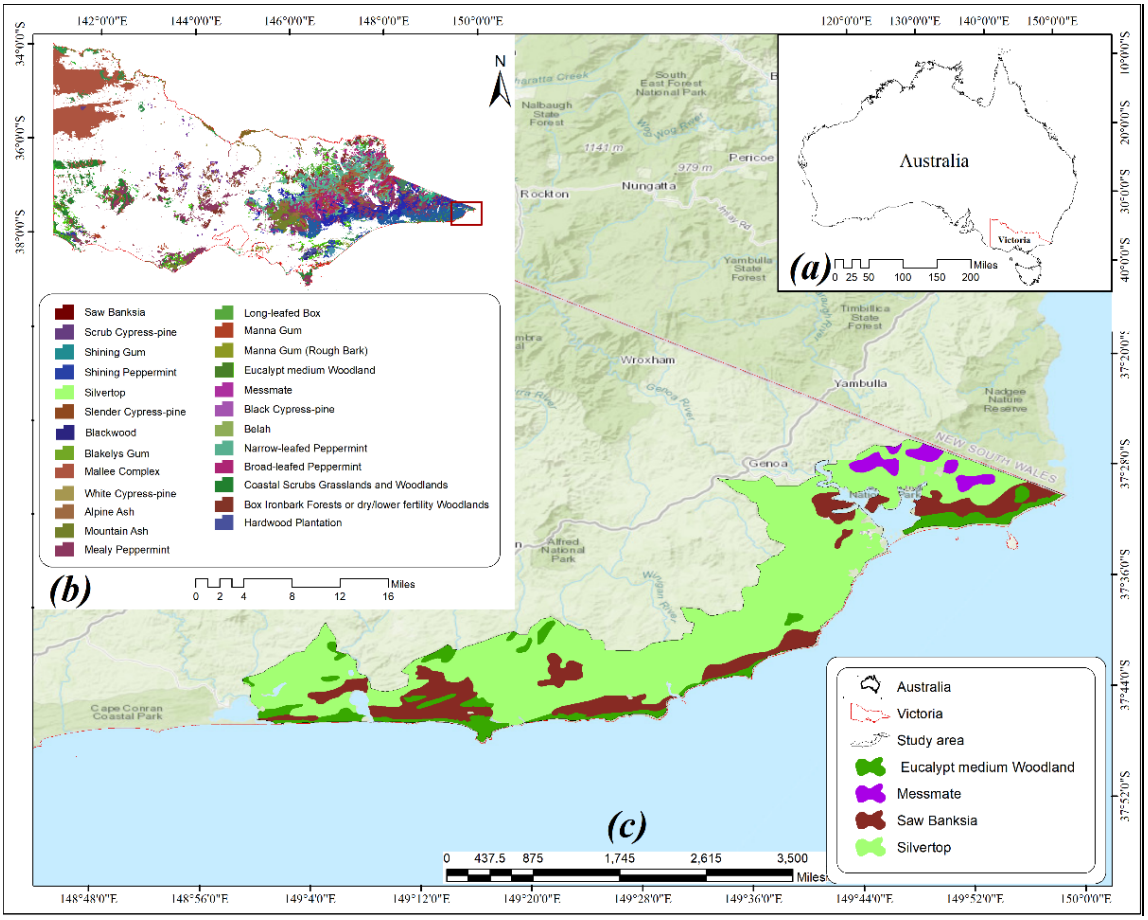

Figure 1. Geographic location of the study area: (**a**) the study area in Australia, (**b**) main forest distribution in Victoria, Australia, and (**c**) geographical location and main forest distribution in the study area.

The goal of the planned burn was to moderate the danger of wildfires by reducing fuel such as dead wood, leaf litter, bark, and shrubs, preventing extreme scorching or defoliation of tree crowns in the forest with young regrowth. The flow diagram in Figure 2 summarizes the approaches developed in this study.

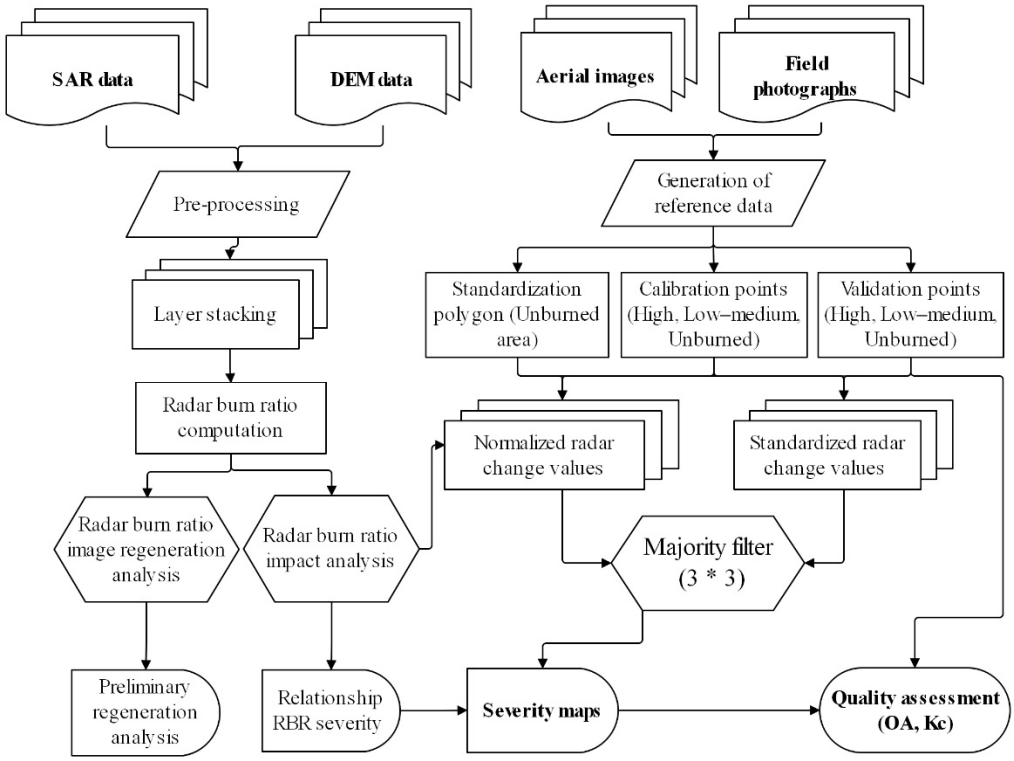

Figure 2. General framework of this study.

3. Materials and Methods

3.1. Radar Data

The Sentinel-1 Single Look Complex (SLC) datasets were obtained from the Copernicus Open Access Hub and used in this study (Table 1). The dual polarization mode of the fine-beam (polarization of VV and VH) datasets (orbit: 29794, frame: 716, path: 147) were collected with a 36.4° incident angle at the middle of the swath. For burn severity estimation, two SAR images (6 October 2019 and 22 February 2020) obtained under different environmental conditions (dry and wet) were used. The post-fire tree growth was examined using a third SAR imagery dataset (18 October 2020), which was collected ten months after the fire (Table 1). Sentinel-1 datasets were obtained over the same season (austral-autumn) to reduce the possible variations caused by plant phenology and to ensure that environmental settings are as comparable as possible.

Table 1. The obtained SAR data and cumulative precipitation (mm) three days prior to image acquisition. Historical median values for temperature and precipitation over the study period are also provided.

SAR Acquisition Dates	Timing	Mission Identifier	Mode/ Beam	Product Type	Polarization	Cumulative Precipitations (mm)			
						Point Hicks	Genoa	Mallaoooota	Gabo Island Lighthouse
Fire occurrence data	29 November 2019								
Pre-fire	06 October 2019	S1A	IW	SLC	VV/VH	33 [a]	16.3 [a]	38.5 [a]	36.9 [a]
Post-fire	22 February 2020	S1A	IW	SLC	VV/VH	0 [b]	4.0 [b]	11.3 [b]	28.5 [b]
Post-fire tree regrowth	18 October 2020	S1B	IW	SLC	VV/VH	20.8 [a]	21.8 [a]	9.3 [a]	26.8 [a]

[a]: Precipitation registered partially during the acquisition date. [b]: Precipitation reported the following day after image acquisition.

The SLC data were co-registered to the first image of the series (6 October 2019) using a lookup table generated from the images' orbital state vectors. An image-to-image cross-correlation algorithm was used to estimate the residual offsets present in the lookup table [36]. Least square and third-degree polynomial function regression methods were used to solve the errors in the lookup table, and offsets in the table were modeled. Multi-look (eight looks in azimuth and four in range) techniques were applied to the co-registered images to achieve a spatial resolution of 30 m. The SAR intensity data was normalized using an incident field of a derived DEM to achieve the gamma naught backscatter coefficient [3]. Using the Range-Doppler approach, the SAR images were orthorectified to UTM 50S/WGS 84 projection with topography information from DEM and SAR data orbital details as input [37]. The preprocessing steps were mainly performed using ESA'S SNAP8.0.3 software.

After preprocessing, the SAR images were grouped into three stacks, one for each polarization (VH/VV), and one for normalized difference backscatter intensity (NDBI). The NDBI is a normalized ratio between VV and VH backscatter coefficients (Equation (1)). For each image stack, three images collected on different dates were processed.

$$NDBI = \frac{VV - VH}{VV + VH} \tag{1}$$

The radar burn ratio (RBR) basically works as the post- to pre-fire ratio of the backscattering coefficients (Equation (2)):

$$\mathrm{RBR}_{xy} = \frac{\gamma^0 Postfire_{xy}}{\gamma^0 Prefire_{xy}} \tag{2}$$

where xy describes a particular polarization based on VV or VH and $NDBI$, and the normalized backscatter coefficient based on a linear scale is γ^0 (gamma naught). In both dry and wet conditions, the indices of RBR were computed based on the two polarization (VV, VH) images and $NDBI$. The RBR was also computed using the mean of all pre- and post-fire images. Image histograms were analyzed, and the first (1) and last (99) percentiles were masked to eliminate outliers. In total, nine RBR images were created.

3.2. Reference Data

A total of 139 geo-located field photographs and an aerial orthophoto with 17 cm spatial resolution were used to create reference data (i.e., 730 points of different severity levels). The orthophoto was taken on 22 February 2020 (two months after the burn) with a Hasselblad H4D-60 camera and georeferenced and orthorectified by Parks and Wildlife Service, WA. Field images were taken between September and October 2020 (ten months after the fire) and corresponded to areas with varying levels of effects. Parks and Wildlife Service from the Department of Agriculture provided the aerial image and field photos. We further explain three burn severity levels and regrowth of vegetation in Figure 3.

(I) Unburnt class: The prescribed burn appears to have had little effect on these areas.
(II) Low–medium severity class: Areas where the fires affect only understory vegetation while the crown remains largely unaffected, as well as areas where convective heat from fire scorched the crown but the canopy structure was maintained (most of the leaves and main branches). Due to the difficulty in identifying subtle fire effects through aerial image photointerpretation and the sensitivity of the C-band to the largest structural elements of vegetation, severity levels from low to moderate were considered as a single class (mainly stems and branches). Hence, the C band's ability to distinguish moderately intense thresholds where large canopy elements remain relatively unchanged may be affected.
(III) High severity: The crown canopy is entirely absent, and the main branches are partly burned or missing. There are still several fallen stems.

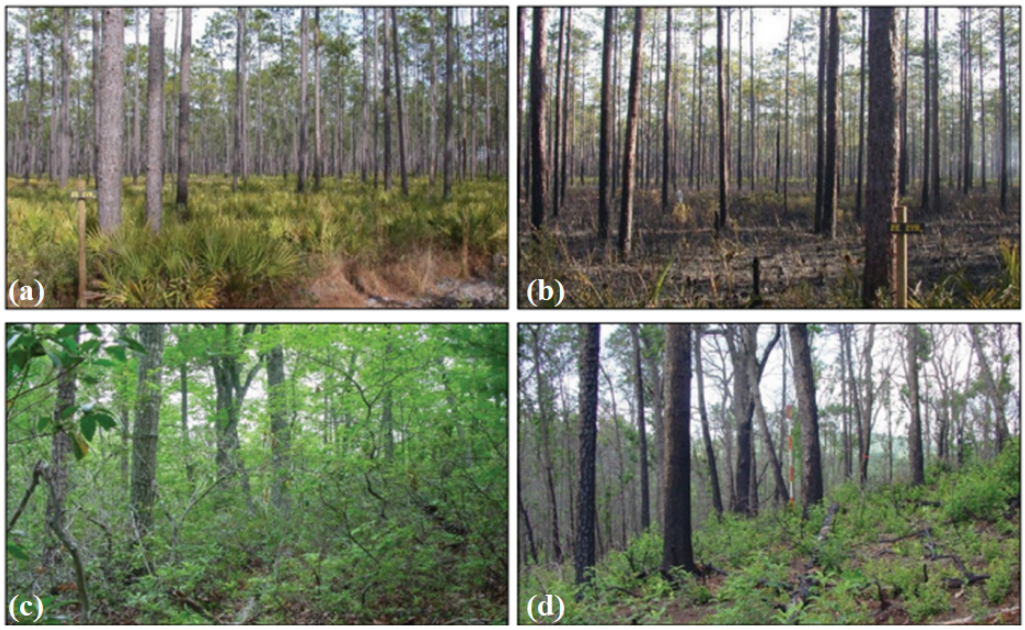

Figure 3. Details of severity levels and regrowth of vegetation in the study area: (**a**) burned area with low to moderate severity, (**b**) burned area with high severity, (**c**) unburned area, and (**d**) regrowth of vegetation.

Within the prescribed burn boundary, a standard point grid with 300 m spacing was used to select the sampling points. While the unburned region within the burn area was small, to represent unburned trees, the points found outside the fire border were also sampled. There were 730 points sampled proportional to the area in each single class. The distribution of sample points was stratified by severity classes. The dataset was divided into two sets after each plot was allocated to a severity class. The first set was used to calibrate the model, while the second was used to validate it. The points for validation were selected randomly, leaving all the unselected points for calibration. The results were not influenced by the various calibration sample sizes for each class, since median value was used for model calibration for every single class.

3.3. Ancillary Data

The Meteorology Bureau, Government of Australia, provided regular precipitation weather data in the nearest four meteorological stations, i.e., Point Hicks (Lighthouse), Genoa (Fools Haven), Mallacoota, and Gabo Island lighthouse (http:/www.bom.gov.au/climate/data/, accessed on 10 May 2021) (Table 1). In order to explain the environmental conditions (dry or wet) related to radar backscatter variability due to changes in soil moisture, the data for cumulative precipitation for the three days prior to the SAR acquisition date were obtained. Low spatial variability of soil moisture in the top few centimeters is related to high temperatures (high evapotranspiration potential) and low precipitation. The dates 6 October 2019 and 22 February 2020 were labeled as dry and wet, respectively. Since the cumulative precipitation was low and the precipitation was registered at least one day before the SAR acquisition date, the image used to assess post-fire tree survival (18 October 2020) was considered dry. The Shuttle Radar Topography Mission Digital Elevation Model (DEM) data with 30 m spatial resolution was used for the orthorectification of SAR data.

3.4. Analysis and Modeling of Prescribed Burns

RBR values were derived for all sample points (dry, wet, mean), taking into consideration each type of polarization/index (VV, VH, and NDBI) with different environmental conditions. To describe the relationship between prescribed burn effects and RBR under different environmental conditions and polarizations, the mean values with standard devi-

ation values were analyzed. Two modeling approaches were combined for the extraction of prescribed burn effects using the RBR images. The first modeling approach was suggested in [29] (the STAND model below). An initial strategy was developed and tested to ease organizational execution (the NORM model). Note that linear scale operations of a mathematical approach were conducted on the SAR images, while a logarithmic scale (base 10) was used for data analysis (decibels, dB), which is a standard procedure in radar remote sensing.

3.4.1. Standard Model (STAND)

There are three continents with seven different forest types included in the original RBR system, translating into the large variations of RBR ranges. By standardization of mathematical data (having z-scores), which rescales the values of RBR to a particular range, compensation for different RBR ranges was achieved. It is important to note that RBR standardization is not exclusively appropriate for the small area examined in this study. The original RBR system, however, was retained for reference purposes. Furthermore, using standard values (z-scores, distance among the significance of the sample values and the mean of the population) is helpful to interpret the RBR values over various environmental conditions. Standardization was carried out using Equation (3):

$$s^{RBR} = \frac{(x - \mu)}{\sigma} \quad (3)$$

where the standardized RBR value is s^{RBR}, x represents the pixel value, and σ and μ are the mean and standard deviation values of RBR applied to adjacent non-fire-affected areas of forest.

For standardization, the unburned pixels were used to show the difference compared to the original process, as the burned region typically displayed gradient ranges from moderate to low, which then leads to the high variability of the backscatter. Every pixel value shows the difference in backscatter present in the pixel and backscatter mean of unburned areas with the use of unburned area for standardization, allowing for better data analysis (the difference with unburned conditions). To measure the μ and σ values, a total of 3524 pixels in 5 polygons across the prescribed burn were used to account for spatial variability in the forest. Once the images with uniform characteristics (s^{RBR}) were collected, for each single image, the mean value of each class related to severity was determined using the backscatter values derived from the calibration dataset coordinates. Thresholds dividing various severity classes were calculated as the median value of the mean (s^{RBR}) of neighboring severity classes [30]. The median was perceived to be a stable central tendency test (where outliers are less sensitive) in the case of SAR image analyses marked with speckle noise.

3.4.2. Normalized Model (NORM)

This model uses the normalized values (n^{RBR}, Equation (4)) of backscattering coefficients. The benefit of using n^{RBR} lies in its simplified calculation and interpretation, as the index does not require standardization:

$$n^{RBR} = \frac{\gamma^0 Postfire_{xy} - \gamma^0 Prefire_{xy}}{\gamma^0 Postfire_{xy} + \gamma^0 Prefire_{xy}} \quad (4)$$

where xy is a definite polarization (i.e., VV or VH) or NDBI, and γ^0 (gamma naught) is the linear-scale normalized backscattering coefficient. As in the previous model, the median values were used for computing thresholds between groups.

3.4.3. Model Validation

Using the thresholds obtained for each model, images were classified using s^{RBR} or n^{RBR}, including unburned, low to medium, and high severity. A total of 18 maps were

produced (Appendix A, Figures A1–A3). In order to minimize the influence of isolated pixels, a major filter (3 × 3) was employed on all maps.

Confusion matrices were constructed using the validity points by removing the modeled fire grades. In order to evaluate the agreement between estimated fire impact and reference, overall accuracy (*OA*), Cohen's kappa (kc), omission error (*OE*), and commission error (*CE*) were calculated using the confusion matrices (Equations (5)–(8)) [38].

$$OA = \frac{TP + TN}{TP + FP + FN + TN} \tag{5}$$

$$kappa = \frac{OA - p_e}{1 - p_e} \tag{6}$$

$$CE = \frac{FP}{TP + FP} \tag{7}$$

$$OE = \frac{FN}{TP + FN} \tag{8}$$

where TP = true positive, TN = true negative, FP = false positive, FN = false negative, and $p_{e=\frac{(TP+FN)\cdot(TP+FP)+(FP+TN)\cdot(FN+TN)}{TP+FP+FN+TN}}$. OA is the total number of accurately predicted values divided by the total number of predictions. The omission error of one class (OE) is the proportion of real samples of that class that were misclassified (they were class A in the ground truth, but we classified them as B, C, or D). The commission error of one class (CE) is the proportion of all classified points in that class that were misclassified (they were classified as class A, but they belong to class B, C, or D in ground truth). The average values of CE and OE in each class were calculated by adding up all false positives, false negatives, true positives, and true negatives. The perception of kappa values relies on various considerations, with no agreement (kc < 0), mild agreement (0 to 0.20), good agreement (0.21 to 0.40), modest agreement (0.41 to 0.60), significant agreement (0.61 to 0.80), and nearly perfect agreement (0.81 to 1) [39].

4. Results

In Figure 4a, RBR_{VH} decreased as the intensity of the fire increased under dry conditions. For the cross-polarized channel between the intensity classes of low to moderate and unburned, an increasing factor in soil moisture due to wet conditions shows a fairly complex relationship with the detection of minor differences. In dry conditions, RBR_{VV} was less effective in distinguishing between fire severity classes but showed the potential under wet conditions to distinguish unburned from burned areas, as explained in Figure 4b. Wet conditions produced the highest dynamic range between unburned and high severity (2 dB) for RBR_{VV}, which may be due to increased backscatter from the field. Under both environmental conditions, the RBR_{NDBI} showed an increase with fire severity, as explained in Figure 4c.

In the process of retrieving the effect based on prescribed burns, two modeling methods produced comparable results. The most reliable predictions were obtained in dry conditions, RBR_{VH}, using the STAND model (OA = 82.3%; kc = 0.78). The results are illustrated in Figure 5.

Figure 6 and Table 2 illustrate validation results for both approaches (STAND and NORM). The gap between the two models was relatively small. Omission and commission errors for the severity class of low to moderate were the largest (30% and 35%, respectively). Errors did not exceed 20% for unburned and high-severity classes. For the cross-polarized pathway (RBR_{VH}), elevated humidity contributed to a significant loss of sensitivity to intensity levels (Table 2). In contrast to the analysis in dry conditions for the cross-polarization channel, RBR_{VV} and RBR_{NDBI} displayed lower OA estimation accuracies (70–80%).

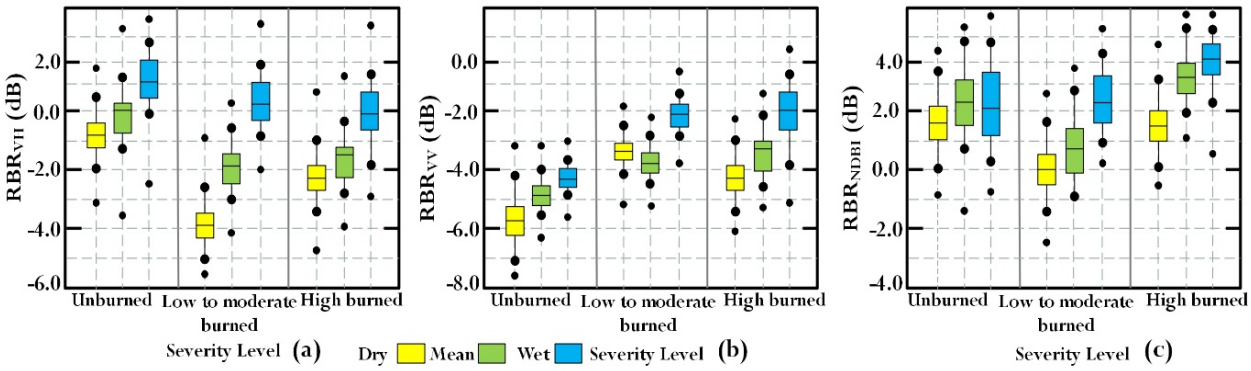

Figure 4. The relationship between RBR and intensity levels under various environmental conditions for VH polarization (**a**), VV polarization (**b**), and NDBI (**c**). Median values (horizontal line), percentiles (25% and 75%, box edges), non-outlier values range (whiskers), and outlier values (circles) are seen in box plots.

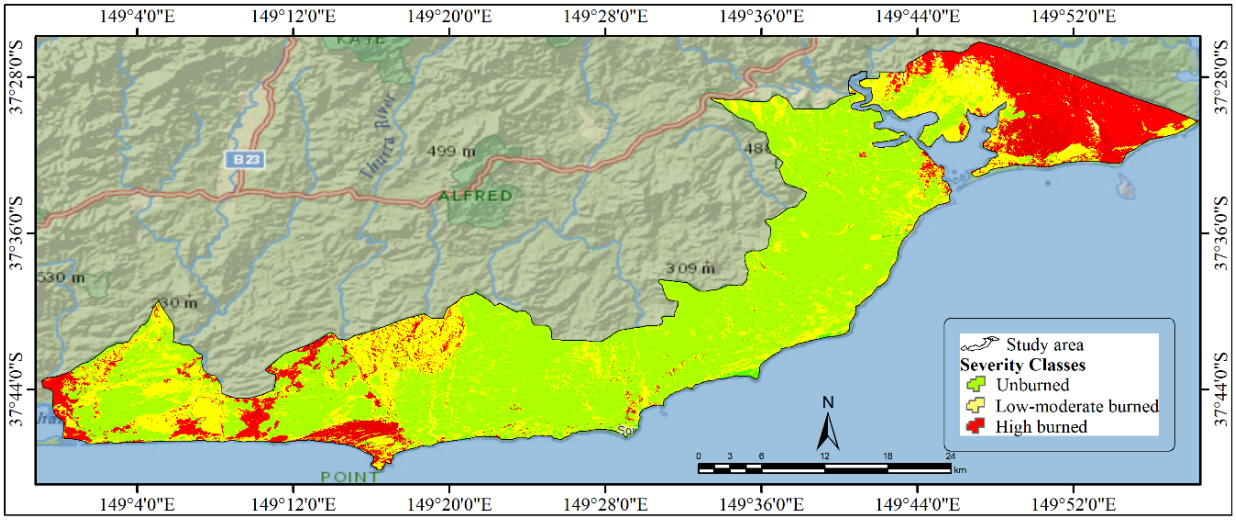

Figure 5. Estimated severity map using VH polarization data in dry conditions and the STAND model.

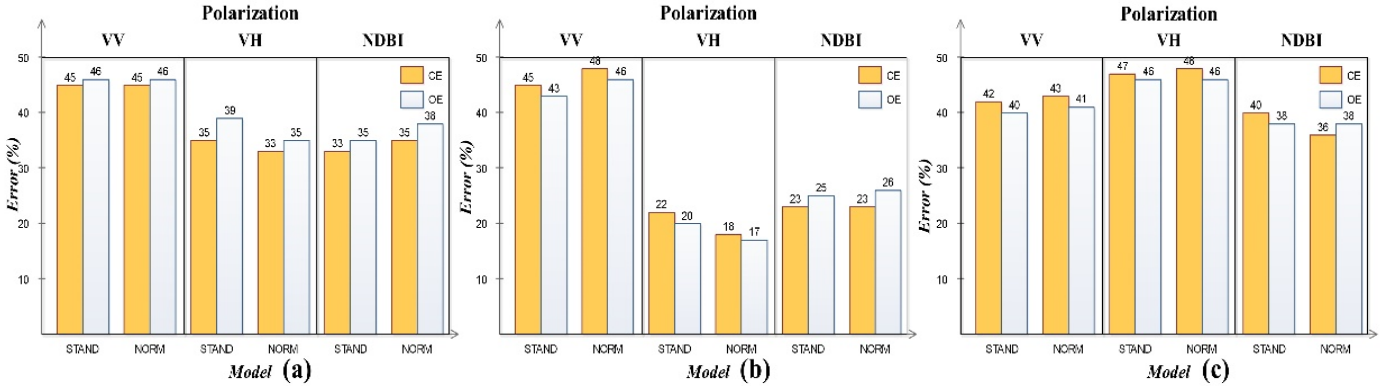

Figure 6. Omission and commission errors (average through classes): (**a**) dry conditions, (**b**) wet conditions, and (**c**) mean conditions.

Table 2. Validation results for severity estimates under different environmental conditions obtained for the VH polarization.

Environmental Condition	Polarization	Model	OA (%)	Kc	Omission Error (%)			Commission Error (%)		
					Low Severity	Low–Medium Severity	High Severity	Low Severity	Low–Medium Severity	High Severity
Wet	VV	STAND	70.0	0.55	18.8	46.0	19.1	13.3	33.3	43.3
		NORM	**76.6**	**0.69**	7.2	32.5	33.6	8.2	35.4	36.5
	VH	STAND	51.2	0.26	8.3	50.8	54.6	35.9	92.5	28.9
		NORM	52.6	0.28	9.3	52.9	56.5	36.7	85.9	30.8
	NDBI	STAND	65.5	0.48	8.3	53.2	16.9	24.5	36.8	51.6
		NORM	60.3	0.50	9.6	52.6	17.8	25.9	23.3	36.6
Dry	VV	STAND	61.1	0.42	9.6	55.3	24.0	36.7	43.3	36.7
		NORM	40.0	0.23	62.5	78.6	50.0	50.0	90.0	40.0
	VH	**STAND**	**82.3**	**0.78**	6.5	35.9	33.9	25.6	42.8	46.6
		NORM	77.2	0.74	27.3	40.7	16.7	20.0	46.7	16.7
	NDBI	STAND	68.9	0.53	20.6	47.4	16.7	10.0	33.3	50.0
		NORM	51.1	0.27	44.2	52.0	54.6	20.0	60.0	66.7
Mean	VV	STAND	60.0	0.40	30.2	60.0	36.4	0.30	66.7	53.3
		NORM	58.9	0.38	34.9	48.2	45.0	6.7	53.3	63.3
	VH	STAND	44.4	0.21	46.7	66.7	63.6	20.0	86.7	60.0
		NORM	**74.4**	**0.62**	25.7	36.0	16.7	13.3	46.7	16.7
	NDBI	STAND	66.7	0.50	15.6	50.0	34.6	10.0	46.7	43.3
		NORM	50.0	0.25	7.4	50.0	52.3	33.3	86.7	30.0

The NORM model outperformed the STAND model for wet images and the mean between dry and wet images (Table 2). Although VH polarization provided the most reliable fire severity forecasts (OA = 82.3%; kc = 0.78) in dry conditions, VV was of particular importance in wet conditions. RBR_{VV} obtained more accurate results than VH and NDBI under wet conditions, with the NORM model showing the least errors (OA = 76.6%; kc =0.69). The NORM model and RBR_{VH} generated the most reliable results (OA = 74.4%; kc = 0.62) for the mean between dry and wet images. It was also possible to differentiate between unburned and burned areas in those circumstances (Appendix A, Figures A1–A3).

5. Discussion

Previous experiments have demonstrated that the impacts of fire can be measured by integrating pre- and post-fire datasets. This study focused on the areas impacted by the incidents of wildfires that are normally marked as high. Our study improves previous knowledge on the accuracy of RBR over prescribed burns to minimize ground fuels with limited effects on the upper canopy. Since C-band SAR data was highly sensitive to scatter from the top part of the canopy [40], the response of RBR to the lower effect levels in areas controlled by prescribed burns should be assessed.

This work proved, even in low to moderate severity, that the cross-polarized channel and dry conditions are the most suitable combination for a fire effect evaluation. The fire sensitivity was found to be poor in the co-polarized channel, specifically in dry conditions, and increased under wet conditions, which is consistent with previous studies using X-, C-, and L-band data over different types of woods [26,28,41]. Since the ground surface shows more susceptibility with increased backscattering, the VV polarization method and NDBI provide the ability to detect burned areas under wet conditions. A simplified modeling technique was applied and yielded comparable accuracies.

The RBR structure and the thresholds suggested in [30] were used to extract severity maps for the study area. The benefit of using a standard calibration for prescribed burns was demonstrated by maps validated using reference data in this study. The calibrated models greatly improved average efficiency from 60% to 82% and the Kappa coefficient ranged from 0.21 to 0.78. Similarly, the overall accuracy exceeded the minimal value required to map the severity of prescribed burns (82.3%) [42]. However, further studies are required to assess the accuracy attained in other forest types and ecosystems. The results obtained in WA are marginally higher compared to approaches based on a high-resolution optical dataset (OA value range of 78–83%) [15]. The application of SAR polarimetric and phase

information and deep learning methods achieved high accuracies for burnt area mapping from Sentinel-1 SAR data [29,31]. Although the accuracies of the proposed method were relatively lower, it might be more suitable for operational forest fire monitoring with the low demand for computational resources. Moreover, the proposed modeling strategy extracted different severity levels of prescribed burns.

Among the limitations of this study, it is important to point out that five levels of fire severity were considered in previous studies [15], although only three classes were included here. For prescribed burns, fewer groups were considered to distinguish between the unburned (failed burns), burning areas at low to moderate severity levels, and burned areas at a high severity level, where crown tree damage or decreasing trends in stems may decrease productivity of the forest. Using fewer groups may affect the outcomes, as simulation techniques could be more stable, and hence the accuracy will increase. As compared to field investigations, another weakness was due to the use of reference data obtained from satellite image interpretation. Such a strategy can produce noise and lead to the reduction in potential for discrimination. In addition, variations in environmental conditions before and after the burn cause uncertainties in remote sensing detection results. The variations in soil moisture in multi-temporal images may inhibit the evaluation of the impact of fire using SAR datasets [43]. By combining multiple SAR images, the impact of environmental variations can be minimized each time before and after a fire event [9,44].

6. Conclusions

This study expanded our knowledge of SAR data for impact assessment of wildfires through an innovative example, prescribed burns. The outcome of prescribed burning was analyzed by estimating fire effects (severity) on forest flora in Victoria, Australia. The freely available Sentinel-1 C-band SAR data, with a 12-day temporal coverage and a 5 m spatial resolution, was applied because of its sensitivity to structural changes in vegetation after forest fires. A fire intensity assessment was carried out for various polarization and environmental conditions using multi-temporary SAR indices. A modeling approach for prescribed burns that can be implemented operationally was developed. The validation results showed that the VH polarization data under dry conditions provided reliable fire severity forecasts with an overall accuracy of 82.3% (kc = 0.78). Although VH polarization provided the most reliable estimation results in dry and mean between dry and wet images, VV polarization data obtained optimal results in wet conditions. Based on our analysis, the NORM models outperformed the STAND models in wet and mean between dry and wet images. The modeling strategy mostly retained the accuracy of the initial RBR method while reducing computational complexity. This study provided a novel technique to assess the effectiveness of controlled burns for forest management and decision-makers in fire-prone areas. The analysis framework could be useful for forest conservation and fire control decision-makers, not only in southeastern Australia, but also in other areas where burning is used as a land management method. Future research will involve the deployment of multiple SAR wavelength channels and the integration of Sentinel-1 data with optical sensor data to further improve fire severity estimates.

Author Contributions: A.T.: Conceptualization, Writing—review and editing, Methodology, Software, Formal analysis, Visualization, Data curation, Writing—original draft, Investigation; H.S.: Supervision, Conceptualization, Writing—review and editing, Methodology, Software, Formal analysis, Visualization, Data curation, Writing—original draft, Investigation; Q.L.: Supervision, Conceptualization, Writing—review and editing, Methodology, Software, Formal analysis, Visualization, Data curation, Writing—original draft, Investigation, Funding; O.A.: Visualization, Validation, Investigation, Writing—review and editing; M.R.K.: Writing—review and editing, Methodology, Formal analysis, Visualization, Investigation; M.F.B.: Visualization, Validation, Investigation, Writing—review and editing; L.L.: Supervision, Writing—review and editing, Methodology, Software, Formal analysis, Visualization, Data curation, Writing—original draft, Investigation, Funding. All authors have read and agreed to the published version of the manuscript.

Funding: This work is supported by the Strategic Priority Research Program of the Chinese Academy of Sciences (Grant No. XDA23100304), the National Natural Science Foundation of China (Grant No. 41871345), and the National Natural Science Foundation of China (Grant No. 42071321).

Data Availability Statement: The data presented in this study are available upon request from the corresponding author. The data are not publicly available due to the thesis that is being prepared from these data.

Acknowledgments: The authors wish to thank the editors and anonymous reviewers for their valuable comments and helpful suggestions. The authors are grateful to GIS Department (Corporate Services | Department of Environment, Land, Water and Planning) for providing data and metadata related to the prescribed burn, from which the reference data used in this work were derived.

Conflicts of Interest: The authors declare no conflict of interest.

Appendix A

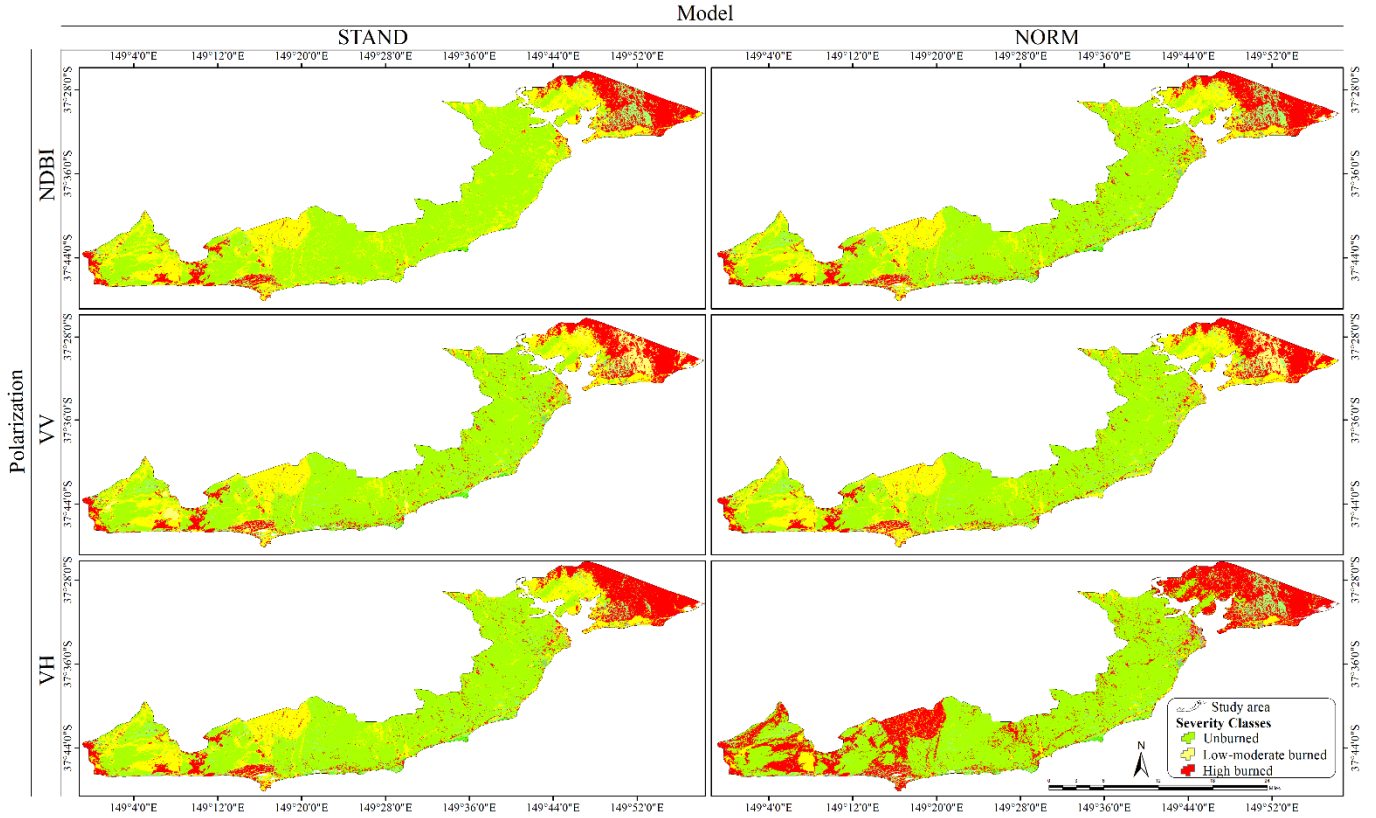

Figure A1. Dry condition.

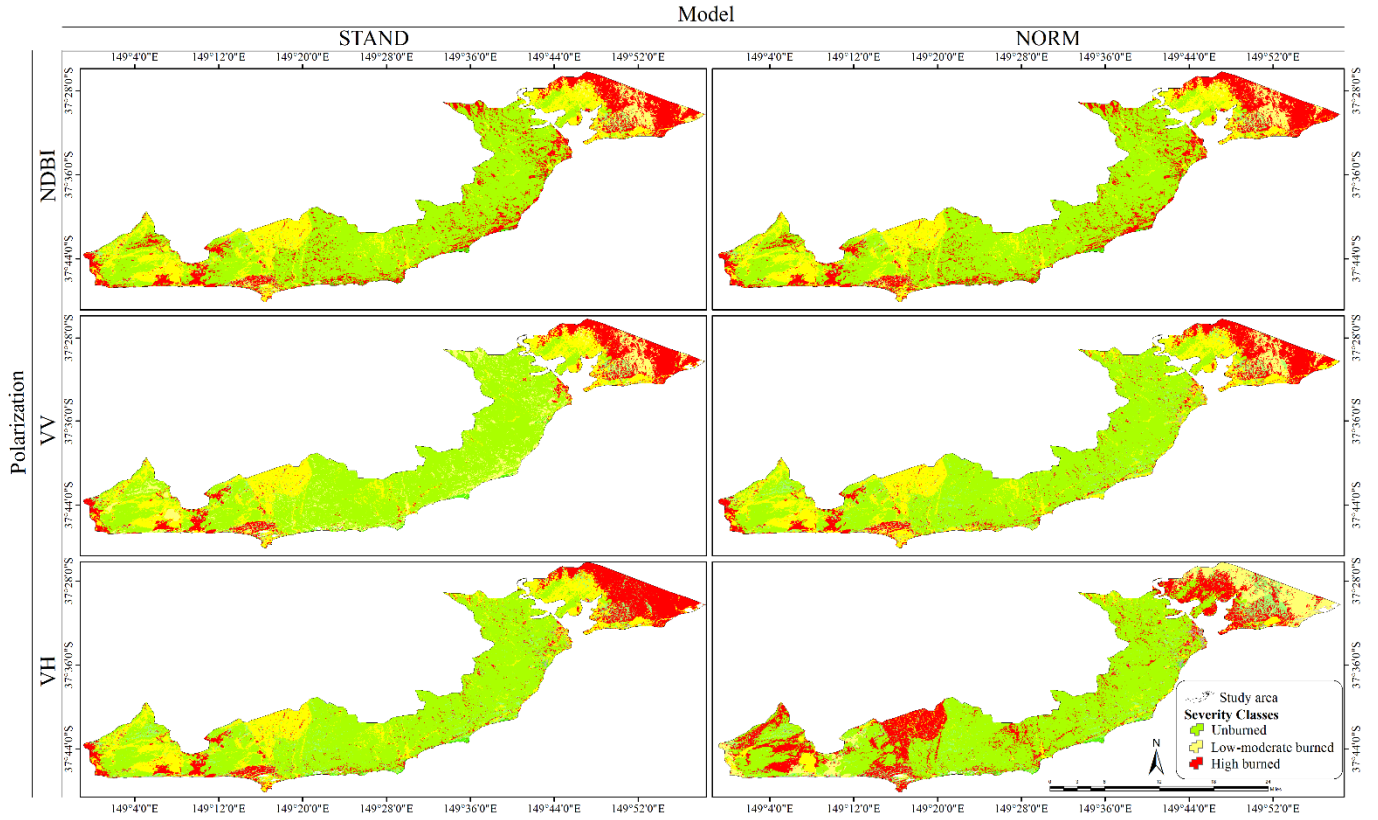

Figure A2. Mean of dry and wet condition.

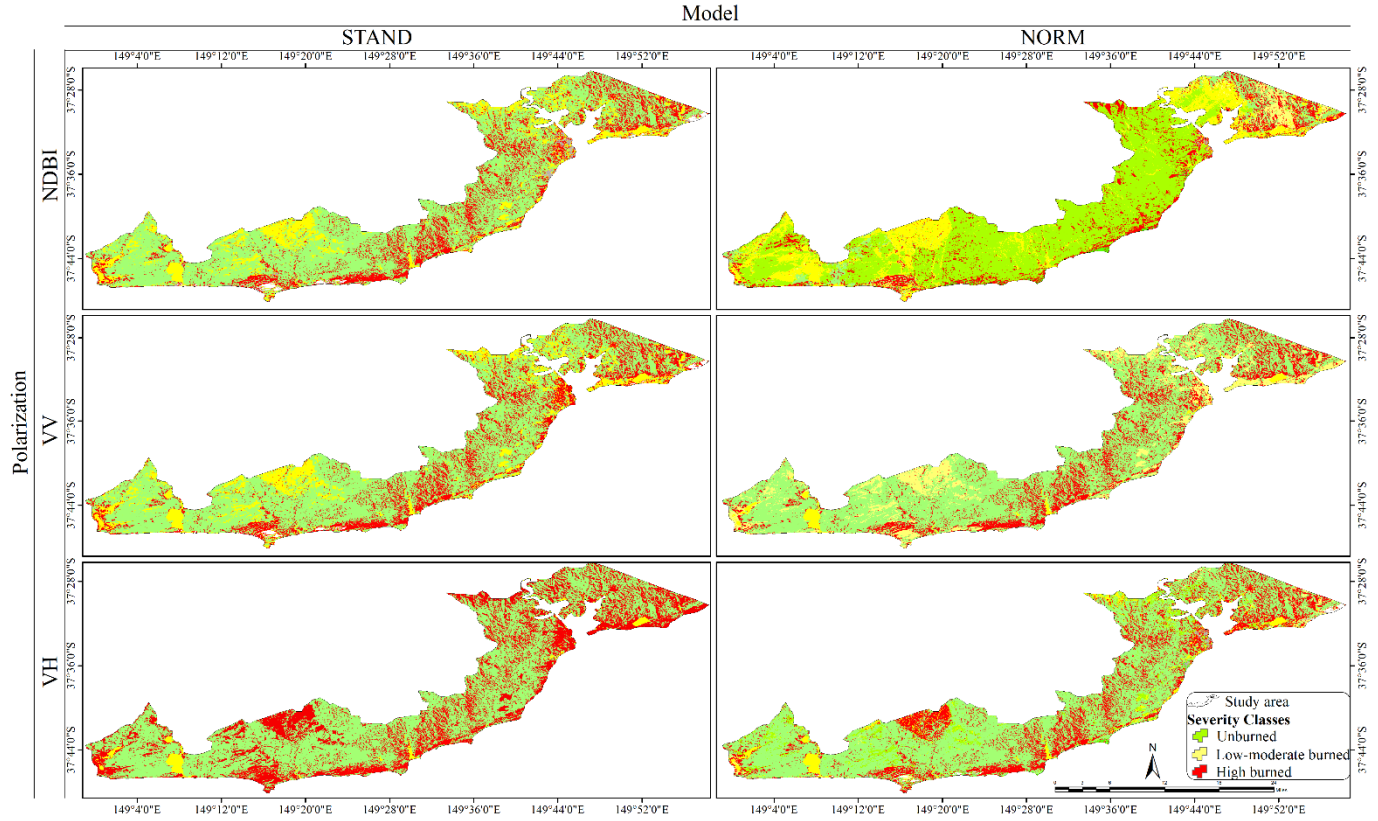

Figure A3. Wet condition.

References

1. Chuvieco, E.; Aguado, I.; Yebra, M.; Nieto, H.; Salas, J.; Martín, M.P.; Vilar, L.; Martínez, J.; Martín, S.; Ibarra, P.; et al. Development of a framework for fire risk assessment using remote sensing and geographic information system technologies. *Ecol. Model.* **2010**, *221*, 46–58. [CrossRef]
2. Kasischke, E.S.; Amiro, B.D.; Barger, N.N.; French, N.H.F.; Goetz, S.J.; Grosse, G.; Harmon, M.E.; Hicke, J.A.; Liu, S.; Masek, J.G. Impacts of disturbance on the terrestrial carbon budget of North America. *J. Geophys. Res. Biogeosci.* **2013**, *118*, 303–316. [CrossRef]
3. McCaw, W.L. Managing forest fuels using prescribed fire—A perspective from southern Australia. *For. Ecol. Manag.* **2013**, *294*, 217–224. [CrossRef]
4. Moreira, F.; Viedma, O.; Arianoutsou, M.; Curt, T.; Koutsias, N.; Rigolot, E.; Barbati, A.; Corona, P.; Vaz, P.; Xanthopoulos, G.; et al. Landscape—wildfire interactions in southern Europe: Implications for landscape management. *J. Environ. Manag.* **2011**, *92*, 2389–2402. [CrossRef] [PubMed]
5. Tariq, A.; Shu, H.; Siddiqui, S.; Munir, I.; Sharifi, A.; Li, Q.; Lu, L. Spatio-temporal analysis of forest fire events in the Margalla Hills, Islamabad, Pakistan using socio-economic and environmental variable data with machine learning methods. *J. For. Res.* **2021**, *13*, 12. [CrossRef]
6. Tariq, A.; Shu, H.; Saddiqui, S.; Mousa, B.G.; Munir, I.; Nasri, A.; Waqas, H.; Baqa, M.F.; Lu, L. Forest fire Monitoring using spatial-statistical and Geo-spatial analysis of factors determining Forest fire in Margalla Hills, Islamabad, Pakistan. *Geomat. Nat. Hazards Risk* **2021**, *12*, 1212–1233. [CrossRef]
7. Fernandes, P.M.; Botelho, H.S. A review of prescribed burning effectiveness in fire hazard reduction. *Int. J. Wildl. Fire* **2003**, *12*, 117–128. [CrossRef]
8. Fernandes, P.M.; Davies, G.M.; Ascoli, D.; Fernández, C.; Moreira, F.; Rigolot, E.; Stoof, C.R.; Vega, J.A.; Molina, D. Prescribed burning in southern Europe: Developing fire management in a dynamic landscape. *Front. Ecol. Environ.* **2013**, *11*. [CrossRef]
9. Boer, M.M.; Sadler, R.J.; Wittkuhn, R.S.; McCaw, L.; Grierson, P.F. Long-term impacts of prescribed burning on regional extent and incidence of wildfires—Evidence from 50 years of active fire management in SW Australian forests. *For. Ecol. Manag.* **2009**, *259*, 132–142. [CrossRef]
10. Gill, A.M.; McCarthy, M.A. Intervals between prescribed fires in Australia: What intrinsic variation should apply? *Biol. Conserv.* **1998**, *85*, 161–169. [CrossRef]
11. Andersen, A.N.; Cook, G.D.; Corbett, L.K.; Douglas, M.M.; Eager, R.W.; Russell-Smith, J.; Setterfield, S.A.; Williams, R.J.; Woinarski, J.C.Z. Fire frequency and biodiversity conservation in Australian tropical savannas: Implications from the Kapalga fire experiment. *Austral Ecol.* **2005**, *30*, 155–167. [CrossRef]
12. Youngblood, A.; Wright, C.S.; Ottmar, R.D.; McIver, J.D. Changes in fuelbed characteristics and resulting fire potentials after fuel reduction treatments in dry forests of the Blue Mountains, northeastern Oregon. *For. Ecol. Manag.* **2008**, *255*, 3151–3169. [CrossRef]
13. Hollis, J.J.; Anderson, W.R.; McCaw, W.L.; Cruz, M.G.; Burrows, N.D.; Ward, B.; Tolhurst, K.G.; Gould, J.S. The effect of fireline intensity on woody fuel consumption in southern Australian eucalypt forest fires. *Aust. For.* **2011**, *74*, 81–96. [CrossRef]
14. Burrows, N.D.; Wardell-Johnson, G.; Ward, B. Post-fire juvenile period of plants in south-west Australia forests and implications for fire management. *J. R. Soc. West. Aust.* **2008**, *91*, 163–174.
15. Loschiavo, J.; Cirulis, B.; Zuo, Y.; Hradsky, B.A.; Di Stefano, J. Mapping prescribed fire severity in south-east Australian eucalypt forests using modelling and satellite imagery: A case study. *Int. J. Wildl. Fire* **2017**, *26*, 491. [CrossRef]
16. Harmon, M.E.; Franklin, J.F.; Swanson, F.J.; Sollins, P.; Gregory, S.V.; Lattin, J.D.; Anderson, N.H.; Cline, S.P.; Aumen, N.G.; Sedell, J.R.; et al. Ecology of Coarse Woody Debris in Temperate Ecosystems. In *Advances in Ecological Research: Classic Papers*; Academic Press: Cambridge, MA, USA, 2004; Volume 34, pp. 59–234. ISBN 0065-2504.
17. Bennett, L.T.; Aponte, C.; Tolhurst, K.G.; Löw, M.; Baker, T.G. Decreases in standing tree-based carbon stocks associated with repeated prescribed fires in a temperate mixed-species eucalypt forest. *For. Ecol. Manag.* **2013**, *306*, 243–255. [CrossRef]
18. Aponte, C.; Tolhurst, K.G.; Bennett, L.T. Repeated prescribed fires decrease stocks and change attributes of coarse woody debris in a temperate eucalypt forest. *Ecol. Appl.* **2014**, *24*, 976–989. [CrossRef] [PubMed]
19. Keeley, J.E. Fire intensity, fire severity and burn severity: A brief review and suggested usage. *Int. J. Wildl. Fire* **2009**, *18*, 116. [CrossRef]
20. Won, M.; Kim, K.; Lee, S. Analysis of Burn Severity in Large-fire Area Using SPOT5 Images and Field Survey Data. *Korean J. Agric. For. Meteorol.* **2014**, *16*, 114–124. [CrossRef]
21. Díaz-Delgado, R.; Lloret, F.; Pons, X. Influence of fire severity on plant regeneration by means of remote sensing imagery. *Int. J. Remote Sens.* **2003**, *24*, 1751–1763. [CrossRef]
22. Lentile, L.B.; Holden, Z.A.; Smith, A.M.S.; Falkowski, M.J.; Hudak, A.T.; Morgan, P.; Lewis, S.A.; Gessler, P.E.; Benson, N.C. Remote sensing techniques to assess active fire characteristics and post-fire effects. *Int. J. Wildl. Fire* **2006**, *15*, 319. [CrossRef]
23. Khriplovich, I.B.; Pomeransky, A.A. Equations of Motion of Spinning Relativistic Particle in Electromagnetic and Gravitational Fields. *Ecol. Appl.* **1998**, *18*, 821–825. [CrossRef]
24. Chu, T.; Guo, X. Remote Sensing Techniques in Monitoring Post-Fire Effects and Patterns of Forest Recovery in Boreal Forest Regions: A Review. *Remote Sens.* **2013**, *6*, 470–520. [CrossRef]
25. Chuvieco, E.; Riaño, D.; Danson, F.M.; Martin, P. Use of a radiative transfer model to simulate the postfire spectral response to burn severity. *J. Geophys. Res. Biogeosci.* **2006**, *111*. [CrossRef]

26. Syphard, A.D.; Keeley, J.E.; Brennan, T.J. Comparing the role of fuel breaks across southern California national forests. *For. Ecol. Manag.* **2011**, *261*, 2038–2048. [CrossRef]
27. Lu, L.; Kuenzer, C.; Wang, C.; Guo, H.; Li, Q. Evaluation of three MODIS-derived vegetation index time series for dryland vegetation dynamics monitoring. *Remote Sens.* **2015**, *7*, 7597–7614. [CrossRef]
28. Stylianidis, E.; Akca, D.; Poli, D.; Hofer, M.; Gruen, A.; Sanchez Martin, V.; Smagas, K.; Walli, A.; Altan, O.; Jimeno, E.; et al. FORSAT: A 3D forest monitoring system for cover mapping and volumetric 3D change detection. *Int. J. Digit. Earth* **2020**, *13*, 854–885. [CrossRef]
29. Engelbrecht, J.; Theron, A.; Vhengani, L.; Kemp, J. A simple normalized difference approach to burnt area mapping using multi-polarisation C-Band SAR. *Remote Sens.* **2017**, *9*, 764. [CrossRef]
30. Tanase, M.A.; Kennedy, R.; Aponte, C. Fire severity estimation from space: A comparison of active and passive sensors and their synergy for different forest types. *Int. J. Wildl. Fire* **2015**, *24*, 1062–1075. [CrossRef]
31. Zhang, P.; Nascetti, A.; Ban, Y.; Gong, M. An implicit radar convolutional burn index for burnt area mapping with Sentinel-1 C-band SAR data. *ISPRS J. Photogramm. Remote Sens.* **2019**, *158*, 50–62. [CrossRef]
32. Schoennagel, T.; Veblen, T.T.; Romme, W.H. The Interaction of Fire, Fuels, and Climate across Rocky Mountain Forests. *Bioscience* **2004**, *54*, 661. [CrossRef]
33. Chou, Y.H.; Minnich, R.A.; Chase, R.A. Mapping probability of fire occurrence in San Jacinto Mountains, California, USA. *Environ. Manag.* **1993**, *17*, 129–140. [CrossRef]
34. Whittaker, J.; Mercer, D. The Victorian bushfires of 2002-03 and the politics of blame: A discourse analysis. *Aust. Geogr.* **2004**, *35*, 259–287. [CrossRef]
35. Bell, D.T.; Plummer, J.A.; Taylor, S.K. Seed germination ecology in southwestern Western Australia. *Bot. Rev.* **1993**, *59*, 24–73. [CrossRef]
36. Wang, Y.; Yu, Q.; Yu, W. An improved Normalized Cross Correlation algorithm for SAR image registration. In *2012 IEEE International Geoscience and Remote Sensing Symposium*; IEEE: Munich, Germany, 2012; pp. 2086–2089.
37. Wegmüller, U.; Werner, C.; Strozzi, T.; Wiesmann, A. Automated and Precise Image Registration Procedures. In Proceedings of the Analysis of Multi-Temporal Remote Sensing Images, Trento, Italy, 13–14 September 2001; World Scientific: Singapore, 2002; Volume 2, pp. 37–49.
38. Cohen, J. Weighted kappa: Nominal scale agreement provision for scaled disagreement or partial credit. *Psychol. Bull.* **1968**, *70*, 213–220. [CrossRef] [PubMed]
39. Landis, J.R.; Koch, G.G. The Measurement of Observer Agreement for Categorical Data. *Biometrics* **1977**, *33*, 159. [CrossRef] [PubMed]
40. Le Toan, T.; Beaudoin, A.; Riom, J.; Guyon, D. Relating forest biomass to SAR data. *IEEE Trans. Geosci. Remote Sens.* **1992**, *30*, 403–411. [CrossRef]
41. Kalogirou, V.; Ferrazzoli, P.; Della Vecchia, A.; Foumelis, M. On the SAR Backscatter of Burned Forests: A Model-Based Study in C-Band, Over Burned Pine Canopies. *IEEE Trans. Geosci. Remote Sens.* **2014**, *52*, 6205–6215. [CrossRef]
42. Jensen, J.R.; Lulla, K. Introductory digital image processing: A remote sensing perspective. *Geocarto Int.* **1987**, *2*, 65. [CrossRef]
43. Kasischke, E.S.; Bourgeau-Chavez, L.L.; Johnstone, J.F. Assessing spatial and temporal variations in surface soil moisture in fire-disturbed black spruce forests in Interior Alaska using spaceborne synthetic aperture radar imagery—Implications for post-fire tree recruitment. *Remote Sens. Environ.* **2007**, *108*, 42–58. [CrossRef]
44. Quegan, S.; Le Toan, T.; Yu, J.J.; Ribbes, F.; Floury, N. Multitemporal ERS SAR analysis applied to forest mapping. *IEEE Trans. Geosci. Remote Sens.* **2000**, *38*, 741–753. [CrossRef]